Electrochemical effects of ALD surface modification on combustion synthesized LiNi$_{1/3}$Mn$_{1/3}$Co$_{1/3}$O$_2$ as a layered-cathode material

Leah A. Riley [a,b], Sky Van Atta [c], Andrew S. Cavanagh [d], Yanfa Yan [b], Steven M. George [e], Ping Liu [c], Anne C. Dillon [b], Se-Hee Lee [a,*]

[a] Department of Mechanical Engineering, University of Colorado at Boulder, Boulder, CO 80309, USA
[b] National Renewable Energy Laboratory, 1617 Cole Boulevard, Golden, CO 80401, USA
[c] HRL Laboratories, LLC, 3011 Malibu Canyon Road, Malibu, CA 90265-4797, USA
[d] Department of Physics, University of Colorado, Boulder, CO 80309, USA
[e] Department of Chemistry and Biochemistry and Department of Chemical and Biological Engineering, University of Colorado at Boulder, Boulder, CO 80309-0215, USA

ARTICLE INFO

ABSTRACT

Combustion synthesized Li(Ni$_{1/3}$Mn$_{1/3}$Co$_{1/3}$)O$_2$ particles are coated with thin, conformal layers of Al$_2$O$_3$ by atomic layer deposition (ALD). XRD, Raman, and FTIR are used to confirm that no change to the bulk, local structure occurs after coating. Electrochemical impedance spectroscopy (EIS) results indicate that the surface of the Li(Ni$_{1/3}$Mn$_{1/3}$Co$_{1/3}$)O$_2$ are protected from dissolution and HF attack after only 4-layers, or ~8.8 Å of alumina. Electrochemical performance at an upper cutoff of 4.5 V is greatly enhanced after the growth of Al$_2$O$_3$ surface film. Capacity retention is increased from 65% to 91% after 100 cycles at a rate of C/2 with the addition of only two atomic layers. Due to the conformal coating, the effects on Li(Ni$_{1/3}$Mn$_{1/3}$Co$_{1/3}$)O$_2$ overpotential and capacity are negligible below six ALD-layers. We propose that the use of ALD for coating on Li(Ni$_{1/3}$Mn$_{1/3}$Co$_{1/3}$)O$_2$ particles makes the material a stronger replacement candidate for LiCoO$_2$ as a positive electrode in lithium ion batteries.

© 2010 Elsevier B.V. All rights reserved.

1. Introduction

In the past few years, there has been a large influx of papers published on replacements for LiCoO$_2$ cathodes. Despite of its stability and high rate capability, LiCoO$_2$ is plagued by issues such as the toxicity and high cost of Co. To address these issues, Co has been both partially and fully replaced with Ni and/or Mn. One viable LiCoO$_2$ replacement material is Li(Ni$_{1/3}$Mn$_{1/3}$Co$_{1/3}$)O$_2$ layered structures.

A variety of fabrication techniques have been used to yield Li(Ni$_{1/3}$Mn$_{1/3}$Co$_{1/3}$)O$_2$. Ohzuku et al. produced pure Li(Ni$_{1/3}$Mn$_{1/3}$Co$_{1/3}$)O$_2$ with a first cycle capacity of 165 mAh g^{-1} using a solid state reaction [1]. Later, Park et al. employed spray pyrolysis in order to achieve a more uniform, homogeneous distribution of nanospherical particles [2]. High purity, spray pyrolysis Li(Ni$_{1/3}$Mn$_{1/3}$Co$_{1/3}$)O$_2$ also performed well at high temperatures (173 mAh g^{-1}) while maintaining cycle stability (94% after 50 cycles). More recently, Sclar et al. reported on Li(Ni$_{1/3}$Mn$_{1/3}$Co$_{1/3}$)O$_2$ fabrication by self-combustion reac-

tion. By tailoring the temperature during an annealing process, Sclar improved both the capacity and the rate capability of Li(Ni$_{1/3}$Mn$_{1/3}$Co$_{1/3}$)O$_2$ [3].

Despite performance gains through changes in synthesis methods, high surface area metal oxides continue to strongly react with standard electrolyte solutions [3]. One quick solution is to prevent electrolyte/electrode interfacial reactions through the application of passive surface coatings. A variety of coatings, such as ZrO$_2$, Al(OH)$_3$, CeO$_2$, and SnPO$_4$ have recently been shown to improve both the thermal stability and the rate capability of Li(Ni$_{1/3}$Mn$_{1/3}$Co$_{1/3}$)O$_2$ [4–8]. However, Al$_2$O$_3$ continues to be the most popular protective surface coating due to the high abundance of aluminum, the low cost of materials, and ease of film deposition. Al$_2$O$_3$ has been successfully applied on high voltage cathode materials such as LiCoO$_2$, LiMnO$_2$, and even Li(Ni$_{1/3}$Mn$_{1/3}$Co$_{1/3}$)O$_2$ [9–12]. These films are normally grown using wet-chemical methods. Myung et al. speculates that Al$_2$O$_3$ may act as a "scavenger" of F$^-$ ions through the formation of Al–O–F and Al–F layers, limiting the concentration of harmful HF species [13].

However, with the exception of Martha et al. and Sclar et al., authors tend not to publish data well-beyond 50 cycles and up to 4.5 V, making the long term reversibility of Li(Ni$_{1/3}$Mn$_{1/3}$Co$_{1/3}$)O$_2$ questionable as a replacement for the widely-used LiCoO$_2$. Likewise, surface films grown using most wet-chemical techniques

either (i) are unable to grow a uniform thin film, (ii) operate at high temperatures or (iii) require long growth time. In order to help improve the electrochemical performance of $Li(Ni_{1/3}Mn_{1/3}Co_{1/3})O_2$, we have chosen to use atomic layer deposition (ALD) to provide controllable, thin, uniform, conformal surface coverage rapidly and at a low temperature of ~180 °C [14].

Here we report large gains in cycle stability through the growth of alumina directly on combustion synthesized (900 °C anneal) $Li(Ni_{1/3}Mn_{1/3}Co_{1/3})O_2$ powders using ALD. With as little as 4 Å of Al_2O_3, we increased stability and decreased resistance, with minimal change to overpotential and rate capability. We show that the conformal, thin coating of alumina on $Li(Ni_{1/3}Mn_{1/3}Co_{1/3})O_2$ by ALD is one of the more promising commercial replacements for $LiCoO_2$.

2. Experimental

2.1. $LiNi_{1/3}Mn_{1/3}Co_{1/3}O_2$ combustion synthesis

The reactants are measured out according to the reaction:

$$LiNO_3 + (1/3)Ni(NO_3)_2 \cdot 6H_2O + (1/3)Co(NO_3)_2 \cdot 6H_2O$$

$$+ (1/3)Mn(NO_3)_2 \cdot 6H_2O + 1.5 \cdot (7/24)C_{12}H_{22}O_{11}$$
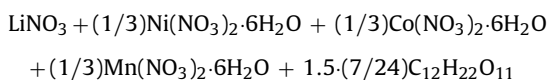
The nitrates are placed in a large dish and melted together with stirring in an inert atmosphere. The mixture is allowed to cool and solidify and is then ground into a paste. The sucrose is added along with a small amount of water to facilitate mixing. The final mixture is a thick, red syrup. The mixture is combusted in one of two ways. The mixture, in a shallow dish, is introduced into a 300 °C furnace or the mixture, in a beaker, is introduced into a preheated 300 °C beaker heating mantle. The volume of the dish or beaker must be many times larger than the volume of the syrup. The dish or beaker is covered with a larger beaker up-ended on supports. All combustion is performed with appropriate exhaust handling. After a few minutes the mixture combusts, the power to the furnace or mantle is terminated, and the setup is allowed to cool. The resulting fine, dark brown powder is collected and annealed for 22 h at either 700 °C or 900 °C (heating rate of 5 °C min^{-1}). The final sample is characterized by X-ray diffraction, scanning electron microscopy, and electrochemical cycling.

2.2. Surface film deposition

Alumina surface films were grown on $LiNi_{1/3}Mn_{1/3}Co_{1/3}O_2$ particles using a rotary ALD reactor [15]. The powders were placed in a porous stainless steel cylinder in the reaction chamber. The cylinder was positioned on a magnetically coupled shaft via a load lock door. A rotor turned the cylinder to agitate the powder and doses of trimethylalumina (TMA) and water were alternated to yield thin conformal alumina coatings. A capacitance manometer was used to measure the pressure in the reaction chamber. The introduction of precursor and purge gases was controlled via a series of pneumatic and needle valves. To evacuate the chamber, a gate valve was opened to connect the chamber to a vacuum pump.

2.3. Electrode fabrication

Electrochemical tests were performed in a CR-2032 coin cell configuration with lithium foil as a counter electrode. The fabrication process was identical for bare and ALD coated $LiNi_{1/3}Mn_{1/3}Co_{1/3}O_2$ powders. Composite electrodes were comprised of $LiNi_{1/3}Mn_{1/3}Co_{1/3}O_2$ active material, acetylene black (Alfa Aesar, AB) as a conductive additive, and Kynar polyvinyldene fluoride (PVDF) binder in a weight ratio of (83:7.5:9.5). The composite was mechanically spread onto high-grade alumina foil current collector using a notch bar. To ensure complete electrical contact and

to improve energy density, electrodes were calendared to 75% of the initial thickness. To remove excess water, electrodes were dried in air at 80 °C for 1 h and in a vacuum oven overnight at 150 °C. The separators were thick porous silica and the electrolyte was 1 M $LiPF_6$ in EC:DMC (1:1 volume ratio).

2.4. Material characterization

Transmission electron microscopy was performed using a FEI Tecnai F20 UT microscope operated at 200 kV. Elemental analysis of the active material and surface film was confirmed by nano-probe energy dispersive X-ray spectroscopy (EDS). Bare $LiNi_{1/3}Mn_{1/3}Co_{1/3}O_2$ was examined in a Hitachi S-4800 Field Emission SEM. A small amount of each sample was dispersed on a conductive carbon tape, and imaged using a low accelerating voltage (<5 kV) and a fast scan rate during image acquisition in an effort to minimize the effects of sample charging. No conductive coating was applied to the sample material. Nicolet 510 FT-IR Spectrometer was used to collect Fourier transform infrared (FTIR) spectroscopy data. Due to the opacity of the electrode, the reflectivity of the samples was measured using a single beam method. Excess water and CO_2 was purged with nitrogen for at least 20 min prior to background collection in order to minimize signal contamination. The spectrometer was run at an average of 256 scans between 4000 and 400 cm^{-1} at a resolution of 4 cm^{-1}. Raman shift of $Li(Ni_{1/3}Mn_{1/3}Co_{1/3})O_2$ powders were collected on a JASCO NRS-3100 at 0.8 mW for 532 nm.

2.5. Electrochemical testing

All assembled cells were allowed to rest for at least 12 h at room temperature, though no more than 24 h, prior to electrochemical testing. Stability tests were cycled between 3.0 and 4.5 V using a constant current–constant voltage (CCCV) profile consisting charge/discharge current density of 40 mA g^{-1} (corresponding to ~C/4) for the first two formation cycles, an increase to 200 mA g^{-1} (corresponding to ~1.25 C) for subsequent cycles, and a 1 h voltage hold at 4.5 V. Rate studies were tested (3.0–4.5 V) using a symmetric galvanostatic profile with the current systematically increased (40–50–80–200–400–800–1200–1600 mA g^{-1}) every three cycles. AC impedance was performed using a Solatron 1280 C for a frequency range of 20,000–0.1 Hz. Impedance measurements were taken on every sixth cycle (100 mA g^{-1}) at 3.2 and 4.2 V on both charge and discharge. A 1 h hold prior to measurement was employed to ensure constant voltage. The cyclic voltammogram measurements were taken at a scan rate of 100 μV s^{-1} between 3.0 and 4.6 V.

3. Results and discussion

Combustion synthesis ($T_c = 900$ °C) of $Li(Ni_{1/3}Mn_{1/3}Co_{1/3})O_2$ yields a fine, uniform, black powder. SEM images, shown in Fig. 1 shows the size distribution and the individual particle morphology. Particle size of the bare $Li(Ni_{1/3}Mn_{1/3}Co_{1/3})O_2$ ranges from 200 to 400 nm in diameter. At a lower synthesis temperature of 700 °C, SEM images reveal a decrease in uniformity (not shown). Small, nano-sized particles become intermixed by larger formations made from long, platelet shaped $Li(Ni_{1/3}Mn_{1/3}Co_{1/3})O_2$. Due to size homogeneity, $Li(Ni_{1/3}Mn_{1/3}Co_{1/3})O_2$ synthesized at 900 °C as seen in Fig. 1 was chosen as the active cathode material in this study.

Successful growth of Al_2O_3 on the surface of $Li(Ni_{1/3}Mn_{1/3}Co_{1/3})O_2$ particles is confirmed from Fig. 2. Preceding deposition, the bare surface is smooth with no distinct features present in TEM (Fig. 2a). Further elemental analysis indicates high concentrations of Ni, Mn, Co, and O (Fig. 2c). Additional
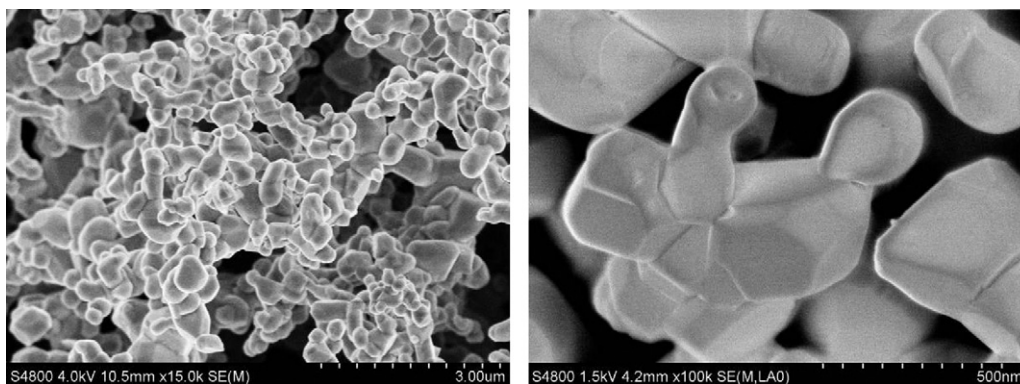
Fig. 1. SEM images of combustion synthesized, bare $Li(Ni_{1/3}Mn_{1/3}Co_{1/3})O_2$ material, annealed at 900 °C.

peaks labeled Cu are due to the copper sample mounting grid. Once alumina as been grown, TEM in Fig. 2b shows a uniform, conformal, white layer covering the $Li(Ni_{1/3}Mn_{1/3}Co_{1/3})O_2$ surface. The conformal, self-limiting nature of ALD is widely accepted for achieving superior growth of thin films and has been evidenced by our group through the successful cycling of Al_2O_3-coated graphite in propylene carbonate (PC) electrolyte [16,17]. The difference in TEM contrast between the surface film and the bulk $Li(Ni_{1/3}Mn_{1/3}Co_{1/3})O_2$ is attributed to compositional differences after coating. EDS (Fig. 2d) supports the presence of aluminum along the surface of the Al_2O_3-coated sample that is not found in the bare sample. The metal peaks in the Al_2O_3-$Li(Ni_{1/3}Mn_{1/3}Co_{1/3})O_2$ identified by EDS remain similar in relative intensity to bare $Li(Ni_{1/3}Mn_{1/3}Co_{1/3})O_2$ and are a strong indicator that the ALD process does not change the elemental composition of the local structure. Unlike the metal counts, the relative intensity of oxygen after ALD increases by nearly 50% along the particle surface. Both the appearance of Al and the increase in O validates that the white coating visible by TEM is the ALD grown Al_2O_3 surface film.

The XRD pattern for bare and alumina coated combustion synthesized $Li(Ni_{1/3}Mn_{1/3}Co_{1/3})O_2$ is shown in Fig. 3. The material is a highly crystalline layered structure, with diffraction peaks cor-
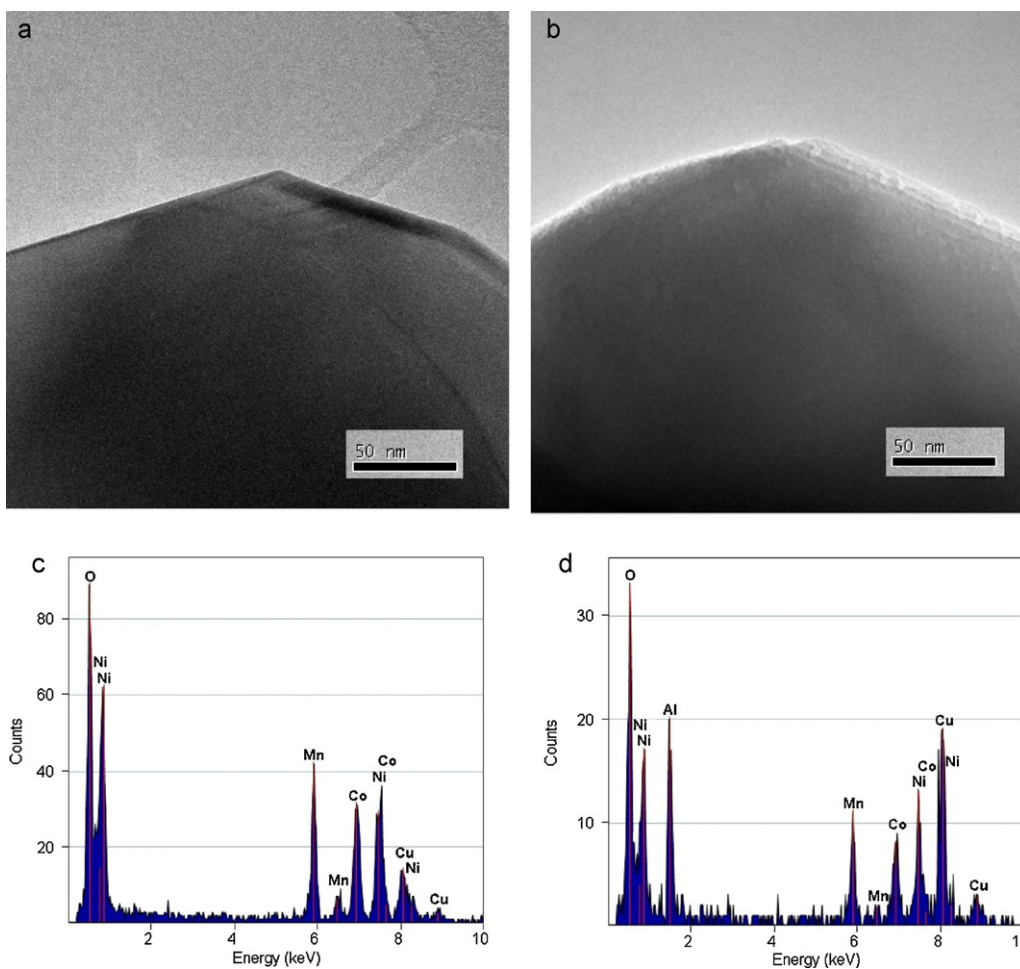
Fig. 2. TEM image of (a) bare and (b) Al_2O_3 coated $Li(Ni_{1/3}Mn_{1/3}Co_{1/3})O_2$. EDS elemental analysis spectra taken on the surface of (c) bare and (d) Al_2O_3 $Li(Ni_{1/3}Mn_{1/3}Co_{1/3})O_2$ particle shown in TEM.

Table 1
Lattice constants and structural properties of bare and alumina coated $Li(Ni_{1/3}Mn_{1/3}Co_{1/3})O_2$ particles.

Sample	a (Å)	c (Å)	c/a	V (Å^3)	$I(003)/I(104)$	R-factor
Bare $Li(Ni_{1/3}Mn_{1/3}Co_{1/3})O_2$	2.863	14.219	4.97	100.94	1.25	0.52
Al_2O_3-coated $Li(Ni_{1/3}Mn_{1/3}Co_{1/3})O_2$	2.860	14.231	4.98	100.80	1.30	0.49
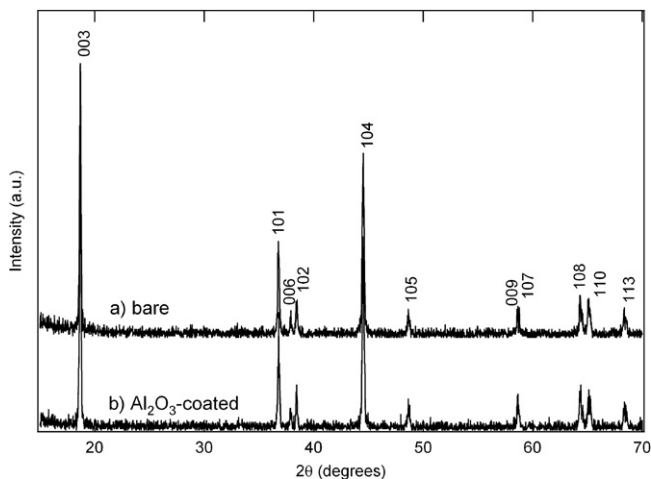
Fig. 3. XRD spectra of (a) bare and (b) alumina coated $Li(Ni_{1/3}Mn_{1/3}Co_{1/3})O_2$ particles.

responding to the R-3m space group (1 6 6). The alumina coating (Fig. 3b) grown by ALD is amorphous and yields minimal changes to the material structure. Table 1 summarizes characterization differences between the bare and ALD coated $Li(Ni_{1/3}Mn_{1/3}Co_{1/3})O_2$. The splitting of the (1 0 8), (1 1 0) and (0 0 6), (1 0 2) peaks seen in XRD as well as an integrated ratio of $I(0 0 3)/I(1 0 4) > 1.2$ indicate a well-ordered α-NaFeO$_2$ structure, with limited cation mixing [3].

Selective regions of Raman and FT-IR are shown in Fig. 4. Similar to XRD, alumina is assumed to be inactive for Raman and IR at low wavenumbers [18,19]. We assume that the structure of $Li(Ni_{1/3}Mn_{1/3}Co_{1/3})O_2$ is layered with a space group of R-3m, similar to that of LiCoO$_2$. Therefore, the corresponding optical vibrational modes are: $\Gamma = A_{2g} + E_g + 2A_{2u} + 2E_u$ [20]. The first two modes are

visible only by Raman while the second two modes can be measured with IR. In theory, two Raman bands and four IR bands, two for each mode, should be visible. The active M–O symmetrical stretching and bending vibrational Raman modes of A_{1g} and E_g are labeled accordingly in Fig. 4a. Both samples clearly show the two active Raman modes. Bare $Li(Ni_{1/3}Mn_{1/3}Co_{1/3})O_2$ Raman peaks appear slightly broader compared to after ALD-coating. Peak broadening, commonly accompanied by a red shift, can be associated with increased structural disorder caused by the different cation–anion bond lengths of the metals [21,22]. The clear absence of a red shift in A_{1g} and E_g, suggests that the subtle broadening differences are due to sample focus and large relative spot size ($\sim$2 μm vs. 500 nm particles). For both samples, a small shoulder in near 640 cm^{-1} is visible that is not inherent to the Raman vibrational modes for a layered structure. A band at 630 cm^{-1} may strongly correlate to the F_{2g} mode of a cubic spinel structure as often found in LiMn$_2$O$_4$ [23]. However, a spinel structure (Fd3m space group) has three vibrational modes and four defined Raman bands ($\Gamma_{ram.} = A_{1g} + E_g + 2F_{2g}$) between 400 and 700 cm^{-1} [20]. Since a fourth peak is not visible in either of the Raman samples, we can assume that the presence of this feature does not indicate a local spinel structure. An alternate explanation is that the Raman shoulder may be due to the inherent disorder complex-layered structures compared to simple-layered structures, such as LiCoO$_2$. As explained above, the structural disorder found naturally in poly-metal oxide structures has been shown to broaden Raman peaks. As the disorder increases, the symmetry may in turn decrease. Li et al. predicted that the additional Raman mode may be an artifact from this lowered symmetry [21]. The second two optical observable modes, A_{2u} and E_u, consist of four bands visible by IR – three of which can be seen between 400 and 800 cm^{-1}. The change in IR spectra due to alumina surface coating is identical to that recorded by Ref. [24]. Prior to an alumina coating, the bare $Li(Ni_{1/3}Mn_{1/3}Co_{1/3})O_2$ shows two clear peaks ($\sim$540 and 610 cm^{-1}) corresponding to the M–O stretching and O–M–O
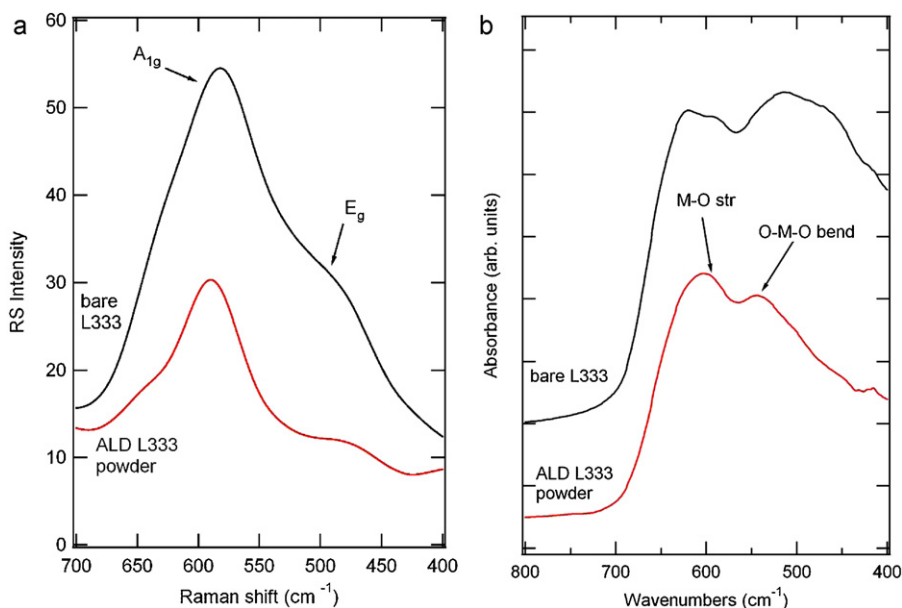
Fig. 4. (a) Raman spectra and (b) FT-IR spectra of bare and ALD coated $Li(Ni_{1/3}Mn_{1/3}Co_{1/3})O_2$ powder.

bending. A smaller feature at 425 cm^{-1} is the only visible LiO$_6$ line in the given range. As seen in both Raman and FTIR, and supported by XRD, even though the ALD coating alters the surface chemistry, the local structure remains constant.

Fig. 5 compares the steady-state cyclic voltammogram (CV) for bare, 4-, 6-, and 10-layers of Al$_2$O$_3$, at a rate of 100 µV s^{-1}. Typical of Li(Ni$_{1/3}$Mn$_{1/3}$Co$_{1/3}$)O$_2$, the bare sample displays a sharp cathodic peak at 3.90 V followed by a broader anodic feature during delithiation at 3.71 V. The bare peak separation potential is 190 mV. As expected, for 4- and 6-layers of alumina (Fig. 5b and c), the cathode peak is shifted to a higher overpotential of 3.91 and 3.92 V, respectively. When the particles are coated, surface kinetics associated with both charge transfer and lithium ion diffusion through the alumina slow, resulting in an increase in polarization [9]. Peak separation potentials increase to 200 mV (5% increase) for 4-layers of alumina and 210 mV (10% increase) for 6-layers of alumina. Surprisingly, despite the positive shift in the cathodic peak potential, no significant change in anodic peak potential is observed with 4- and 6-layers of alumina. Change in the anodic peak potential is not evident until 10-layers of alumina are grown on the Li(Ni$_{1/3}$Mn$_{1/3}$Co$_{1/3}$)O$_2$ nanoparticles (Fig. 5d). The reduced ionic mobility accompanied by a 10-layer thick alumina coating decreases the anodic peak to 3.69 V and increases the total peak separation potential to 300 mV (58% increase).

The stability enhancement of the ALD coating is most visible from the electrochemical performance (Fig. 6a). After two cycles, the current rate was increased from 40 mA g^{-1} to 200 mA g^{-1} at room temperature (1C = 160 mA g^{-1}). The bare Li(Ni$_{1/3}$Mn$_{1/3}$Co$_{1/3}$)O$_2$ displays a stable capacity of ~150 mAh g^{-1} for 15 cycle, after which the capacity begins to steadily drop, retaining only 103 mAh g^{-1} by the 100th cycle. However, upon the application of 2-ALD layers of Al$_2$O$_3$, the Li(Ni$_{1/3}$Mn$_{1/3}$Co$_{1/3}$)O$_2$ retains 140 mAh g^{-1} after 100 cycles and exhibits little change in initial capacity. Similar improvements are also observable when the coating thickness is increased to 4- and 6-layers. For thicker films, the decrease in first cycle specific capacity can be associated with slower ionic mobility through the Al$_2$O$_3$ to reach the Li(Ni$_{1/3}$Mn$_{1/3}$Co$_{1/3}$)O$_2$ surface. Despite a lower initial capacity due to slower ionic mobility through the Al$_2$O$_3$ layer, the capacity after 40 and 70 cycles of 4- and 6-Al$_2$O$_3$ Li(Ni$_{1/3}$Mn$_{1/3}$Co$_{1/3}$)O$_2$ is greater than the bare due the improved electrochemical stability. Of the ALD coatings tested, only 10-Al$_2$O$_3$ is found to be detrimental to the overall performance of Li(Ni$_{1/3}$Mn$_{1/3}$Co$_{1/3}$)O$_2$. Since alumina is a both an electronic and ionic insulator, the thicker coating tends to physically isolate individual particles from direct contact with conductive acetylene black. Fig. 5b further examines the effect ALD coating thickness on Li(Ni$_{1/3}$Mn$_{1/3}$Co$_{1/3}$)O$_2$ capacity retention when cycled with an upper cutoff of 4.5 V. The capacity retention was measured after 20, 40 and 110 cycles for coated samples. ALD–Al$_2$O$_3$ thicknesses were based upon a deposition rate of ~2 Å cycle^{-1}, as reported by Groner et al. using a variable-angle spectroscopic ellipsometer [25]. The data was then fit with an exponential curve. 2-, 4-, and 6-layers of ALD grown alumina all remain electrochemically stable by retaining >80% of their initial capac-
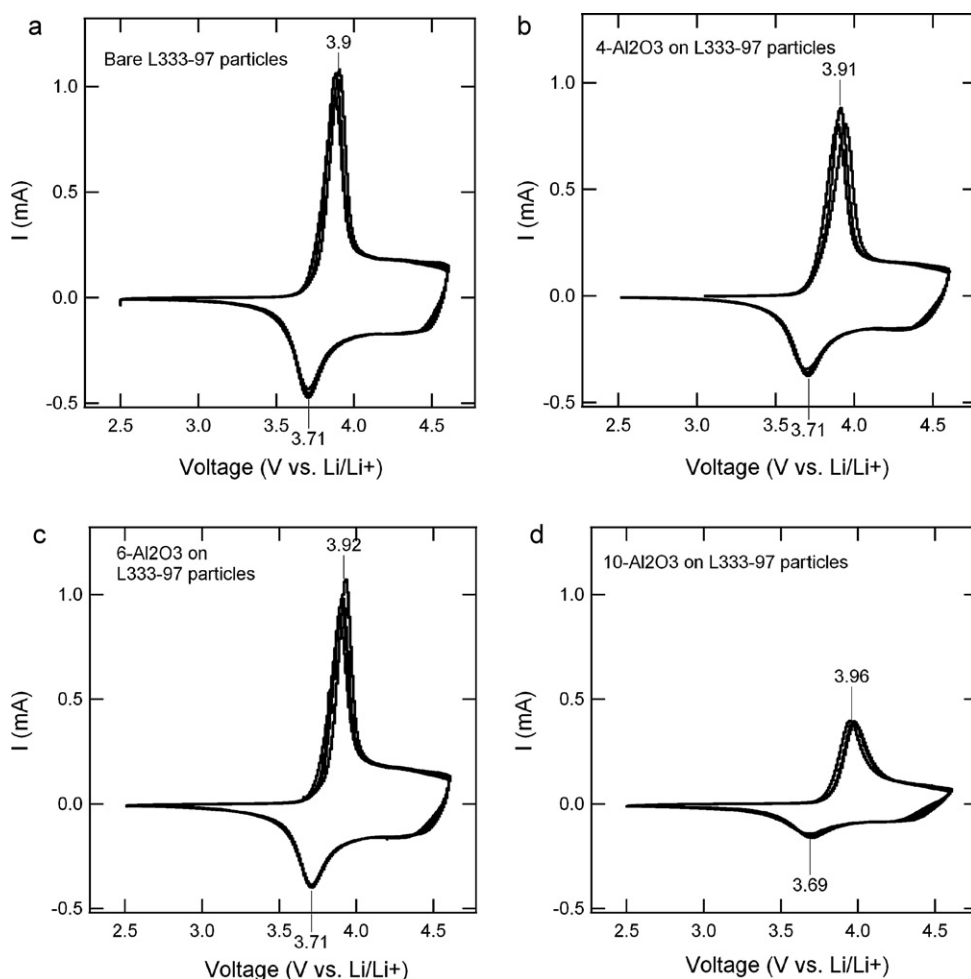
Fig. 5. Steady-state, cyclic voltammogram of (a) bare, (b) 4-Al$_2$O$_3$ Li(Ni$_{1/3}$Mn$_{1/3}$Co$_{1/3}$)O$_2$, and (c) 6-Al$_2$O$_3$ Li(Ni$_{1/3}$Mn$_{1/3}$Co$_{1/3}$)O$_2$, and (d) 10-A$_2$O$_3$ Li(Ni$_{1/3}$Mn$_{1/3}$Co$_{1/3}$)O$_2$ at a scan rate of 100 µV s^{-1} between 2.5 and 4.6 V.

Fig. 7. Rate capability comparison between bare and 4-Al$_2$O$_3$ Li(Ni$_{1/3}$Mn$_{1/3}$Co$_{1/3}$)O$_2$. A rate of 1 C is assumed to be equivalent to a current density of 160 mA g^{-1}.
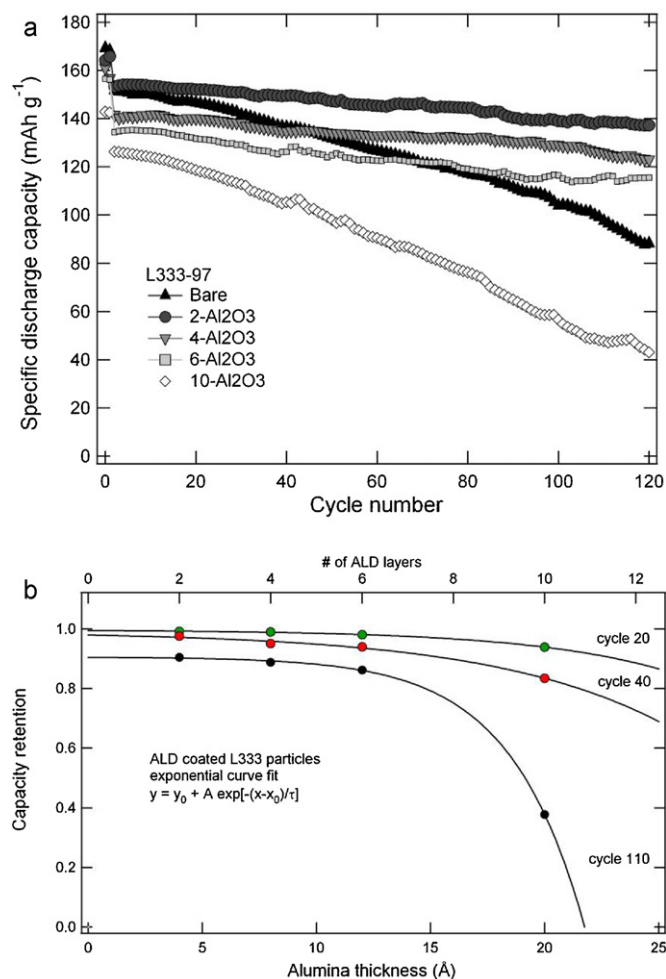
Fig. 6. (a) Electrochemical performance and stability results for bare and alumina coated Li(Ni$_{1/3}$Mn$_{1/3}$Co$_{1/3}$)O$_2$ nanoparticles at room temperature. (b) Capacity retention as a function of alumina film thickness measured during electrochemical testing at specific cycles.

ity after 110 cycles. Once the coating thickness exceeds ∼12 Å, the electrochemical stability is significantly affected by kinetics associated with ion and electron transport. However, similar to previous studies on ALD coated LiCoO$_2$, graphite, and MoO$_3$, our maximum allowed thickness (1.2 nm) is significantly less than all other coatings grown using other deposition methods [9,26,27]. Alumina coatings grown by wet-chemical techniques with thickness of 4 nm, 5 nm, and even 20–30 nm (∼20 times greater than ALD maximum thickness) displayed notable improvements in stability after 40 cycles [12,13,28]. At the time, we are unable to provide a concrete explanation for the difference in performance as a function of coating method. Possible factors include differences in density of the grown films, diffusion of aluminum into the active material at high temperatures, film defects and impurities, and coverage area. However, it is clear that the high purity and conformal nature of Al$_2$O$_3$ grown by ALD is able to protect material surfaces by using less material than conventional deposition techniques.

Rate capability of bare and 4-Al$_2$O$_3$ coated Li(Ni$_{1/3}$Mn$_{1/3}$Co$_{1/3}$)O$_2$ is shown in Fig. 7. The rate performance of the bare sample is found to be comparable to recently reported Li(Ni$_{1/3}$Mn$_{1/3}$Co$_{1/3}$)O$_2$ combustion synthesis with a 900 °C anneal [3]. Even at a rate of 2.5 C (400 mA g^{-1}), our bare sample maintains a capacity of 120 mAh g^{-1}. The high rate capability of bare Li(Ni$_{1/3}$Mn$_{1/3}$Co$_{1/3}$)O$_2$ is attributed to the small particle size. Similar to results in a reported study by Hu et al., the alumina
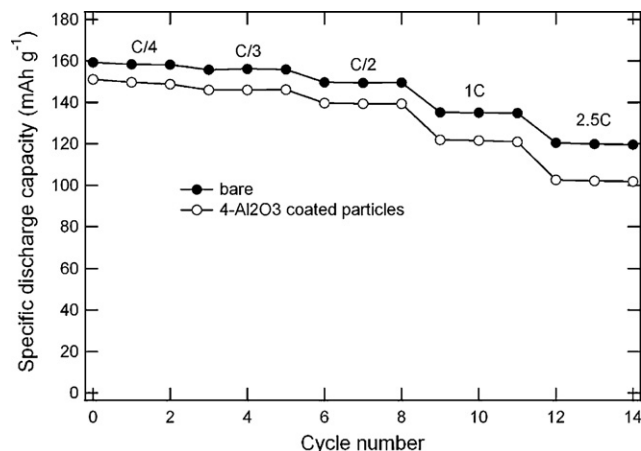
coating improves total stability and cycle life, though produces a small decrease in capacity at higher rates when compared to bare samples [5]. We can conclude that the maximum capacity at high rates for bare Li(Ni$_{1/3}$Mn$_{1/3}$Co$_{1/3}$)O$_2$ nanoparticles is determined by the bulk material properties, such as the coefficient of diffusion, and not on surface degradation mechanisms. After ALD coating, the alumina serves as a barrier to ion mobility which decreases the total capacity. This is especially evident at higher rates as the capacity difference increases between bare and ALD coated samples.

The failure of high voltage cathodes is normally attributed to dissolution or the side reaction between the liquid electrolyte and the active material [29]. In order to further explain the electrochemical performance results, electrochemical impedance spectroscopy (EIS) measurements were recorded after lithium extraction for 100 cycles (4.2 V). Fig. 8 shows the Nyquist plots for bare and Al$_2$O$_3$ coated Li(Ni$_{1/3}$Mn$_{1/3}$Co$_{1/3}$)O$_2$. Frequency increases from right to left, with the inset depicting the high frequency region of the bare sample, consisting of two overlapping semicircles. The Nyquist is divided into distinct sections and labeled in Fig. 8a as (i) the ohmic resistance of the liquid electrolyte (R_{sol}), (ii) the impedance of the natural and artificial solid electrolyte interface ($R_{sf}||C_{sf}$), (iii) the impedance of electrons through the active material ($R_b||C_b$), (iv) the charge-transfer resistance and the double layer capacitance ($R_{ct}||C_{dl}$), and (v) the impedance to the solid-state diffusion of lithium (Z_W), as introduced by Warburg [30,31]. Sections (ii) and (iii) are considered the high frequency region (HFR), (iv) as the mid frequency region (MFR), and (v) as the low frequency region (LFR). The scale for Fig. 1a and b are identical in order to provide a more accurate visual comparison between the bare and the alumina coated Li(Ni$_{1/3}$Mn$_{1/3}$Co$_{1/3}$)O$_2$. For $R||C$ impedance features, the resistance is closely related to the circle diameter. The most prominent difference between Fig. 8a and b is in the charge-transfer impedance feature (iv).

The impedance spectra were fit to the equivalent circuit model seen in Fig. 8c. The model consists of a series of frequency-independent circuit elements, each one identified as a component on the Nyquist. Due to non homogeneity of the composite, capacitor elements were replaced with constant phase elements (CPE). The impedance for CPE is defined as $Z_{CPE} = 1/B(j\omega)^n$, where ω is angular frequency, j is an imaginary unit, B is a constant, and n represents the distortional effects due to non homogeneity of the electrode surface. As n approaches a value of 1, the frequency response of a CPE is equivalent to that of a capacitor, where $B \rightarrow C$. Impedance for the Warburg-like element is defined by $Z_W = A_w\omega^{-1/2}(1-j)$,
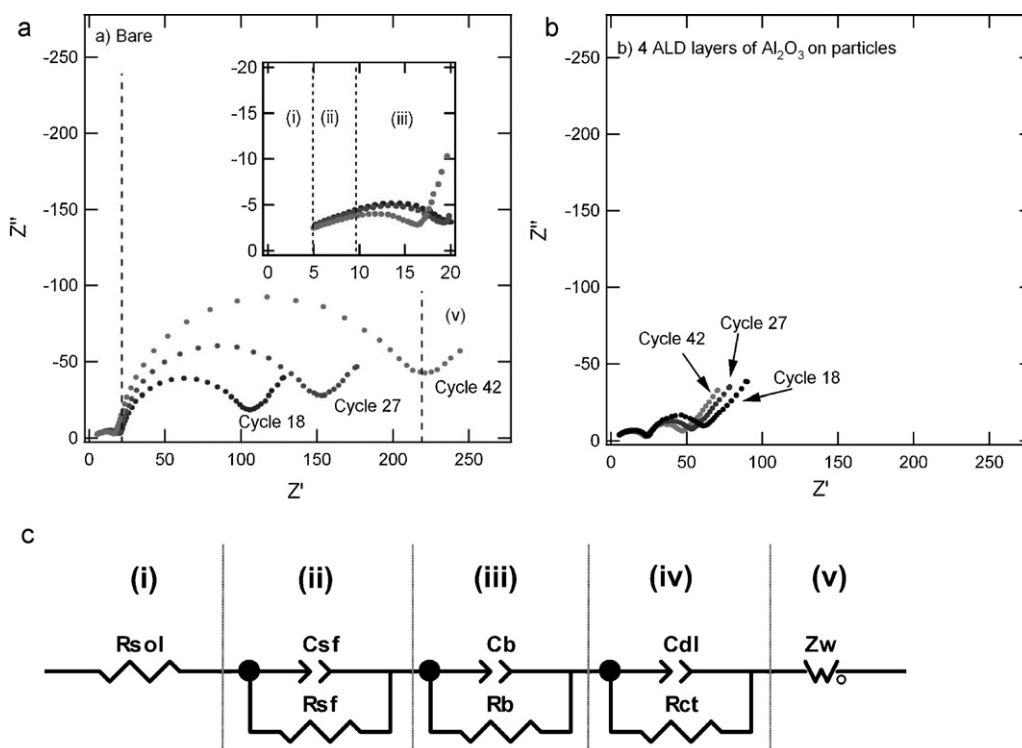
Fig. 8. Electrochemical impedance spectroscopy (EIS) Nyquist plots of (a) bare and (b) 4-Al_2O_3 Li($Ni_{1/3}Mn_{1/3}Co_{1/3}$)O_2. Z'' indicates the imaginary axis while Z' indicates the real axis. The curves were fit with a (c) Voigt-type equivalent circuit.

where A_w is the Warburg coefficienct [32]. Previously explained by Franceschetti and Macdonald, the proposed Voigt-type circuit model in Fig. 8c can be accurate and used to fit impendence data under loosely couples conditions [33]. So initial parameters were chosen based results from an in-depth study of bare Li($Ni_{1/3}Mn_{1/3}Co_{1/3}$)O_2 by Shaju et al. under the assumption our impedance values would be of similar order of magnitude to those by Shaju [34].

Results of equivalent circuit fitting are depicted in Fig. 9a and b. Trends for R, C, and n during the first 40 cycles of bare Li($Ni_{1/3}Mn_{1/3}Co_{1/3}$)O_2 closely match the results reported by Shaju. The constant values of C_b and n_b indicate no significant changes in porosity [34]. The increase in the bare charge-transfer resistance (R_{ct}) as a function of cycle number is associated to material property changes occurring as a result of electrode/electrolyte dissolution or HF attack. The surface of the bare interface is not
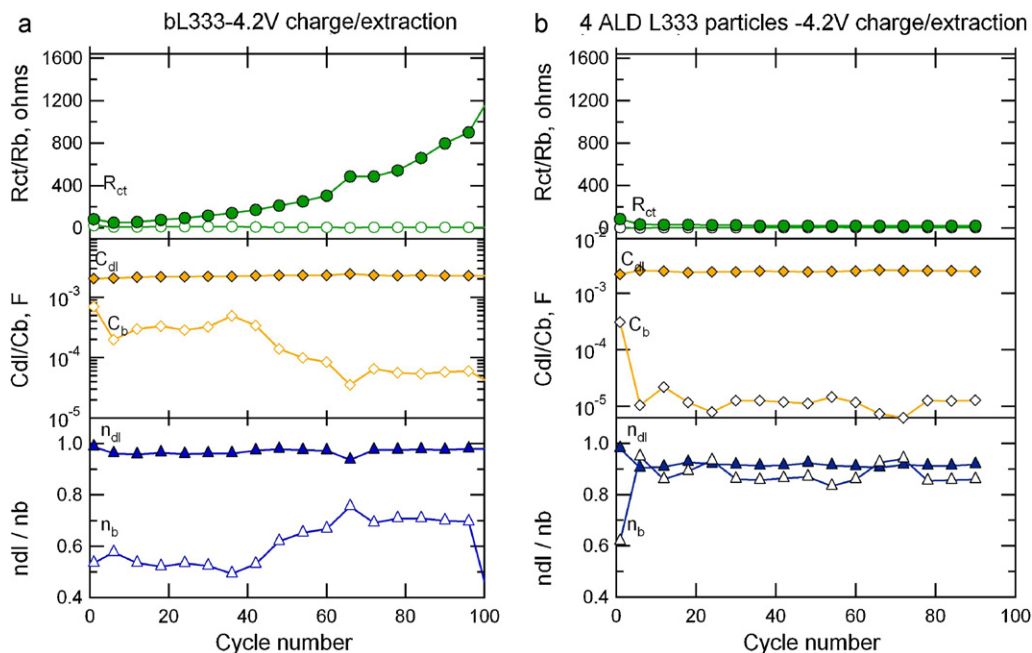
Fig. 9. Equivalent circuit values fit to Fig. 8c for (a) bare Li($Mn_{1/3}Ni_{1/3}Co_{1/3}$)O_2 and (b) 4-Al_2O_3 coated Li($Mn_{1/3}Ni_{1/3}Co_{1/3}$)O_2. Values were collected at 4.2 V on during lithium extraction (charging) after a 1 h voltage hold.

stable in the liquid electrolyte at high voltages. This degradation inhibits the charge transfer at the material surface, causing increase in radius of the R_{ct} semi-circle, seen in Fig. 8. Compared to bare Li(Ni$_{1/3}$Mn$_{1/3}$Co$_{1/3}$)O$_2$, 4-layers of Al$_2$O$_3$ grown on Li(Ni$_{1/3}$Mn$_{1/3}$Co$_{1/3}$)O$_2$ particles yields no change to both the double layer capacitance (C_{dl} and n_{dl}) and the bulk electronic resistance (R_b). More importantly, however, after ALD coating the charge-transfer resistance (R_{ct}) of Li(Ni$_{1/3}$Mn$_{1/3}$Co$_{1/3}$)O$_2$ remains stable as a function of cycle number when compared to the bare sample. The steady value of ALD–R_{ct} is attributed to the added protection of the material from the liquid electrolyte and supports the improved cycling stability seen in Fig. 7.

Despite alumina being an ionic and electronic insulator, extensive studies on LiCoO$_2$ have shown similar EIS results when surface coatings of Al$_2$O$_3$ are converted to a thin layer of Li–Al–Co–O after heat treatment [11]. This layer is found to decrease surface resistance and improve cycle stability. A previous study by Kim et al. showed that the EIS response of alumina-coated Li(Ni$_{1/3}$Mn$_{1/3}$Co$_{1/3}$)O$_2$ particles by sol–gel method is extremely sensitive to the coating thickness [35]. The authors surmise that a heavy coating of 5 wt.% Al$_2$O$_3$ inhibits the movement of Li$^+$ ions while the lighter coating of 3 wt.% Al$_2$O$_3$ provides optimal protection and Li–Al–M–O formation. While similar on many levels, the most notable difference between the sol–gel studies cited and this work is the absence of heat treatment of our ALD-coated particles. In order to form the lithium-bearing surface film through ion migration, sol–gel coated particles need to be heated at temperatures above 500 °C. Thicker films not undergoing heat treatment fail to form a uniform ion conductive surface. ALD-grown Al$_2$O$_3$ does not require heat treatment to obtain improved conductivity. It is suggested that the enhanced performance and lower resistance seen in EIS reported in this work may be attributed to the formation of a lithium-bearing surface film which occurs during electrochemical cycling. Further studies are currently underway to extensively examine the electrochemical evolution of conformal ALD coatings.

4. Conclusion

Here we have shown that conformal and uniform coatings are highly important to performance optimization of Li(Ni$_{1/3}$Mn$_{1/3}$Co$_{1/3}$)O$_2$. Even after 100 cycles, the frequency response of the coated Li(Ni$_{1/3}$Mn$_{1/3}$Co$_{1/3}$)O$_2$ remains unchanged and suitably protected from physical contact with the liquid electrolyte even with only 4 layers of conformal alumina. As evidenced by electrochemical characterizations, the stability and retention of the coated Li(Ni$_{1/3}$Mn$_{1/3}$Co$_{1/3}$)O$_2$ can be greatly improved. Changes to the overpotential are extremely sensitive to film thickness. Large variations in film thickness seen from wet chemical coating methods could create a wide range of potential drops along the surface of a single particle. We believe that only through layer-by-layer controllable coverage, such as ALD, can the maximum efficiency and stability be achieved with minimum addition of non-reactive material.

References

[1] T. Ohzuku, Y. Makimura, Chemistry Letters (2001) 642–643.
[2] S.H. Park, C.S. Yoon, S.G. Kang, H.S. Kim, S.I. Moon, Y.K. Sun, Electrochimica Acta 49 (2004) 557–563.
[3] H. Sclar, D. Kovacheva, E. Zhecheva, R. Stoyanova, R. Lavi, G. Kimmel, J. Grinblat, O. Girshevitz, F. Amalraj, O. Haik, E. Zinigrad, B. Markovsky, D. Aurbach, Journal of the Electrochemical Society 156 (2009) A938–A948.
[4] F. Wu, M. Wang, Y.F. Su, L.Y. Bao, S. Chen, Electrochimica Acta 54 (2009) 6803–6807.
[5] S.K. Hu, G.H. Cheng, M.Y. Cheng, B.J. Hwang, R. Santhanam, Journal of Power Sources 188 (2009) 564–569.
[6] S.B. Jang, S.H. Kang, K. Amine, Y.C. Bae, Y.K. Sun, Electrochimica Acta 50 (2005) 4168–4173.
[7] H.S. Kim, W.S. Kim, H.B. Gu, G. Wang, Journal of New Materials for Electrochemical Systems 12 (2009) 207–212.
[8] Y.Y. Huang, J.T. Chen, J.F. Ni, H.H. Zhou, X.X. Zhang, Journal of Power Sources 188 (2009) 538–545.
[9] Y.S. Jung, A.S. Cavanagh, A.C. Dillon, M.D. Groner, S.M. George, S.H. Lee, Journal of the Electrochemical Society 157 (2010) A75–A81.
[10] X.L. Li, F.Y. Kang, X.D. Bai, W.C. Shen, Journal of Inorganic Materials 22 (2007) 1037–1040.
[11] S. Oh, J.K. Lee, D. Byun, W.I. Cho, B.W. Cho, Journal of Power Sources 132 (2004) 249–255.
[12] J. Cho, Y.J. Kim, T.J. Kim, B. Park, Journal of the Electrochemical Society 149 (2002) A127–A132.
[13] S.T. Myung, K. Izumi, S. Komaba, Y.K. Sun, H. Yashiro, N. Kumagai, Chemistry of Materials 17 (2005) 3695–3704.
[14] S.M. George, A.W. Ott, J.W. Klaus, Journal of Physical Chemistry 100 (1996) 13121–13131.
[15] J.A. McCormick, B.L. Cloutier, A.W. Weimer, S.M. George, Journal of Vacuum Science and Technology A 25 (2007) 67–74.
[16] S.M. George, Chemical Reviews 110 (2010) 111–131.
[17] Y.S. Jung, A.S. Cavanagh, L.A. Riley, S.H. Kang, A.C. Dillon, M.D. Groner, S.M. George, S.H. Lee, Advanced Materials 22 (2010) 2172–2172+.
[18] I.E. Wachs, Catalysis Today 27 (1996) 437–455.
[19] Y. Kurokawa, T. Suga, S. Nakata, T. Ikoma, S. Tero-Kubota, Journal of Materials Science Letters 17 (1998) 275–278.
[20] W.W. Huang, R. Frech, Solid State Ionics 86–88 (1996) 395–400.
[21] X. Li, Y.J. Wei, H. Ehrenberg, F. Du, C.Z. Wang, G. Chen, Solid State Ionics 178 (2008) 1969–1974.
[22] C. Julien, M. Massot, Solid State Ionics 148 (2002) 53–59.
[23] S.J. Hwang, H.S. Park, J.H. Choy, G. Campet, J. Portier, C.W. Kwon, J. Etourneau, Electrochemical and Solid State Letters 4 (2001) A213–A216.
[24] N.V. Kosova, E.T. Devyatkina, Journal of Power Sources 174 (2007) 959–964.
[25] M.D. Groner, F.H. Fabreguette, J.W. Elam, S.M. George, Chemistry of Materials 16 (2004) 639–645.
[26] L.A. Riley, A.S. Cavanagh, S.M. George, Y.S. Jung, Y. Yan, S.-H. Lee, A.C. Dillon, Chemphyschem: A European Journal of Chemical Physics and Physical Chemistry 11 (2010) 2124–2130.
[27] Y.S. Jung, A.S. Cavanagh, L.A. Riley, S.-H. Kang, A.C. Dillon, M.D. Groner, S.M. George, S.-H. Lee, Advanced Materials 22 (2010) 2172–2176.
[28] Z.X. Wang, L.J. Liu, L.Q. Chen, X.J. Huang, Solid State Ionics 148 (2002) 335–342.
[29] P. Arora, R.E. White, M. Doyle, Journal of the Electrochemical Society 145 (1998) 3647–3667.
[30] E. Warburg, Annalen Der Physik 6 (1901) 125–135.
[31] Q.C. Zhuang, J.M. Xu, X.Y. Fan, Q.F. Dong, Y.X. Jiang, L. Huang, S.G. Sun, Chinese Science Bulletin 52 (2007) 1187–1195.
[32] A. Funabiki, M. Inaba, Z. Ogumi, S. Yuasa, J. Otsuji, A. Tasaka, Journal of the Electrochemical Society 145 (1998) 172–178.
[33] D.R. Franceschetti, J.R. Macdonald, Journal of Electroanalytical Chemistry 82 (1977) 271–301.
[34] K.M. Shaju, G.V.S. Rao, B.V.R. Chowdari, Journal of the Electrochemical Society 151 (2004) A1324–A1332.
[35] H.S. Kim, K.T. Kim, Y.S. Kim, S.W. Martin, Metals and Materials International 14 (2008) 105–109.